Scalable nanofabrication of high-quality $YBa_2Cu_3O_{7-\delta}$ nanowires for single-photon detectors

P. Amari,[1,2] S. Kozlov,[1,2] E. Recoba-Pawlowski,[1,2] Z. Velluire-Pellat,[1,2] A. Jouan,[1,2] F. Couëdo,[1,2] C. Ulysse,[3] J. Briatico,[4] D. Roditchev,[1,2] N. Bergeal,[1,2] J. Lesueur,[1,2] and C. Feuillet-Palma[1,2,*]

[1] *Laboratoire de Physique et d'étude des Matériaux, École Supérieure de Physique et de Chimie Industrielles de la Ville de Paris (ESPCI Paris), CNRS, Paris Sciences et Lettres (PSL) University, Paris 75005, France*

[2] *Sorbonne Université, ESPCI Paris, CNRS, Laboratoire de Physique et d'étude des Matériaux, Paris 75005, France*

[3] *Centre de Nanosciences et de Nanotechnologies, C2N CNRS, Université Paris-Saclay, Palaiseau, France*

[4] *Unité Mixte de Physique, CNRS, Thales, Université Paris Saclay, Palaiseau, France*

(Received 4 October 2022; revised 3 August 2023; accepted 14 September 2023; published 10 October 2023)

The realization of superconducting single-photon detectors operating above the liquid-helium temperature is currently the focus of intense research efforts. Here, we present the fabrication of ultraclean encapsulated nanowires from commercially available thin films of $YBa_2Cu_3O_{7-\delta}$ by high-energy oxygen-ion irradiation. The structured nanowires, ranging from 0.1 to 5 μm in width, exhibit sharp resistive transitions to the superconducting state above 85 K. The I-V characteristics reveal that the evolution from the superconducting to the normal state shows a large voltage jump in the volt range. This demonstrates that the entire nanowire transits—a prerequisite for the development of a hot spot upon absorption of a single photon. Our results pave the way for the fabrication of $YBa_2Cu_3O_{7-\delta}$-based scalable superconducting single-photon-detection devices.

DOI: 10.1103/PhysRevApplied.20.044025

I. INTRODUCTION

Single-photon-detector technology has emerged as a building block for numerous applications, including quantum technologies, long-range ($\gg 1$ km [1]), low-light-level imaging, and atmospheric remote sensing. Impressive results have been achieved such as high-rate (1.3 Gbit s^{-1} [2]) and long-distance (404-km [3]), quantum key distribution [4], long-distance quantum communication (> 1200 km [5]), satellite laser ranging [6], high-definition video transmission from space (20 Mbit/s for 239 000 miles [7]), in quantum cryptography and quantum tomography [8]. Original tests of fundamental quantum mechanical properties have been conducted, such as in loophole-free Bell tests [9] and nonclassical single-photon and phonon correlation [10].

There has been significant progress in photomultiplier and avalanche-diode technologies in recent years [11]. It is now possible to detect single photons with very high efficiency in narrow ranges of the electromagnetic spectrum. Nevertheless, such detectors suffer from two main drawbacks. They are usually optimized for UV and visible frequencies and, worse, their dark count is large enough (30 kHz) to significantly affect the signal-to-noise ratio. In addition, their large jitter (500 ps) is deleterious for some applications, such as time-of-flight imaging.

Recently, new detectors have been developed based on a different detection principle and therefore having specific properties. They consist of very thin and narrow wires (typically nanowires that are 4 nm thick, 100 nm wide, and a few tens of micrometers long) of superconducting materials in which a single photon can generate a measurable voltage pulse [12]; hence their name superconducting single-photon detectors (SNSPDs). They operate as follows [13]. A superconducting nanowire is biased just below its critical current. When a photon with energy much higher than the superconducting gap is absorbed, it breaks the Cooper pairs and creates a so-called hot spot. This normal region causes the supercurrents to deviate, so that they spread over the edges of the wire until the critical current density is exceeded. Then, the nanowire locally transits to its resistive state, which generates a voltage pulse. In order to get the highest efficiency, the nanowire has to be thin (a few to a few tens of nanometers thick). Its width has to be of the order of the magnetic penetration length in the superconducting materials (typically 100 nm). To optimize detection efficiency, the detection area is maximized: the nanowire is therefore generally long (from a few hundred microns to a few millimeters) and folded on itself,

*cheryl.palma@espci.fr

 © 2023 American Physical Society

typically in the area of a pixel. Such detectors are wide band, since the mechanism of detection is not based on a specific energy. Moreover, they present a low dark-count rate, since no ionization process is involved in the detection event. Nowadays, SNSPDs based on conventional low-T_c materials such as NbN, Nb-Ti, or WSi [12–15] surpass, in many ways, their semiconductor-based counterparts [15] and are commercially available all around the world [16]. Some tremendous advantages have been reported recently, such as high quantum efficiency (approximately 4% at $\lambda \sim 1.31$ μm [17], 93% at $\lambda \sim 1.55$ μm [18]), a high operating frequency (approximately 1.2 GHz [19]), a low intrinsic dark-count rate (6×10^{-6} counts/s)[20]), low jitter (approximately 4.6 ps full width at half maximum at $\lambda \sim 1.55$ μm [21]) and a broad spectral range (from the visible to the midinfrared [22,23] up to 10-μm wavelength [24]). Very recently, this width constraint has been largely relaxed: single-photon detectors have been realized from thin wires of micron width [25]. However, these devices offer the best performance at ultralow operating temperatures, below 1 K, which requires complex energy-intensive cryogenics and precludes large-scale applications.

In this context, making SNSPDs with high-temperature superconducting materials (HTS SNSPDs) would have two main advantages: the ability to work at higher temperature (around 40 K) with simplified cryogenics and the possibility of operating at higher frequency, due to a 2-orders-of-magnitude-shorter electron-phonon relaxation time [26]. For these reasons, the development of HTS SNSPDs is at the heart of intensive research worldwide [27], based on electron- or hole-doped HTSs such as $Pr_{2-x}Ce_xCuO_{4-\delta}$ [28], $La_{1.85}Sr_{0.15}CuO_4$ [29], $Nd_{2-x}Ce_xCuO_{4\pm\delta}$ [30], $YBa_2Cu_3O_{7-\delta}$ [31–37], $YBa_2Cu_3O_{7-\delta}$-$La_{0.7}Sr_{0.3}MnO_3$ [38], and $Bi_2Sr_2CaCu_2O_{8+\delta}$ [39,40]. Indeed, HTS materials fulfill all the mandatory requirements for detection, such as—for $YBa_2Cu_3O_{7-\delta}$, for instance—a high resistivity, $\rho_{YBa_2Cu_3O_{7-\delta}}$ ($T > T_c$) ∼ 100–300 μΩ cm [31] (comparable to low-temperature superconducting materials used for SNSPD: $\rho_{NbN}(T > T_c) \sim 50$–300 μΩ cm [41,42]), a short coherence length $\xi_{YBCO} \sim 2$ nm ($\xi_{NbN} \sim 5$ nm [43]), an intrinsically fast quasiparticle recombination time (approximately 1 ps [44]), hysteretic *I*-*V* curves [34,44], and, at the same time, a high critical temperature, $T_c \sim 87$ K. These very promising parameters, which would potentially scale up the applications of SNSPDs, must be somewhat balanced by the fact that, according to a recent theoretical publication [45], stringent constraints weigh on the actual realization of a successful device, which we will discuss later on. However, very recently, two groups [39,40] have reported single-photon detection below 25 K from a high-temperature superconducting nanowire, relaunching the race to achieve a single-photon detector operating at around 40 K.

Compared to low-temperature superconductors (LTSs), the growth of ultrathin high-temperature superconducting (HTS) films and their patterning at the nanoscale are major challenges. Indeed, these two steps very often lead to the degradation of the superconducting properties. The $YBa_2Cu_3O_{7-\delta}$ cuprate has a perovskitelike crystal structure in which the superconducting electron transport takes place in CuO_2 planes [46], depending on the oxygen doping. Furthermore, bare $YBa_2Cu_3O_{7-\delta}$ thin films exposed to air easily lose their optimal oxygen doping, mainly due to the ease with which oxygen atoms migrate along the Cu-O [47] chains. Moreover, as the superconducting order parameter has *d*-type wave symmetry [48,49], it results in the presence of nodes in the superconducting gap and makes the material particularly sensitive to the introduction of defects [50]. This creates two major problems for the fabrication of devices with both thickness and width [51–53]. Various techniques have been proposed to overcome these difficulties. One is the use of standard argon-ion etching to shape a wire. This technique requires very careful adjustment of the etching parameters to avoid overheating effects and to limit interaction with the corresponding ions [34]. The edges of the etched wires are favorable areas for oxygen atoms to escape along the Cu-O [47] chains. This affects the superconducting properties, a phenomenon that is amplified for ultrathin films. Protecting the $YBa_2Cu_3O_{7-\delta}$ thin film with a gold layer [54–56] or a 100-nm-thick carbon mask [38,57] significantly limits the detrimental effects of argon-ion etching. These methods improve both the reliability of the fabrication and the homogeneity of the superconducting properties. However, photon detection requires the removal of this protective layer. This additional etching step usually damages the superconducting properties. An alternative approach to argon etching is based on direct etching of the film by a focused ion beam (FIB) of Ga^{3+} [54,58,59]. This method offers higher resolution compared to the usual electron-lithography process. The ion doses used are lower than in conventional Ar etching, thus limiting the introduction of disorder. However, the use of Ga^{3+} ions can damage the superconducting properties of $YBa_2Cu_3O_{7-\delta}$. This is because Ga^{3+} can substitute Cu ions for Cu-O chains, reducing the density of free charge carriers in the CuO_2 planes [60]. In the past decade, a new focused-ion system has emerged, using He^+ ions. This technology offers an interesting alternative, as these neutral ions do not interact with the $YBa_2Cu_3O_{7-\delta}$ thin films [61].

In this paper, we describe a method for fabricating encapsulated HTS nanowires by ion implantation [62,63] that are robust and have excellent superconducting properties. In the METHODS section, we introduce the technique used to fabricate such nanowires by high-energy ion implantation, starting from a $YBa_2Cu_3O_{7-\delta}$ thin film capped by a 8-nm-thick CeO_2 layer. In the second part, we present the different characterizations of the nanowires

by transport measurements in a cryogenic environment. Finally, in the last part, we will study the conditions required to obtain hysteretic *I-V* characteristics with a voltage jump of the order of 1 V.

II. METHODS

The HTS nanowires are fabricated using a high-energy oxygen-ion-irradiation technique combined with electron-beam lithography. In this section, we first describe in detail the ion-implantation technique, which takes advantage of the sensitivity of the $YBa_2Cu_3O_{7-\delta}$ order parameter to defects. Then, we explain the simulation methods that allow the determination of the suitable energy and fluence of the incident ions. Finally, we describe the different steps in the implementation of the ion-irradiation technique used to structure the HTS thin films into superconducting nanowires.

A. Ion implantation

Different techniques exist to implant ions in solid materials, including a FIB method based on, e.g., a gallium [58] or He [61,64] source and wide-beam ion implantation, which is used for *n* or *p* doping in the semiconductor industry [65]. In the latter, selected ions are extracted from a source and then accelerated toward the thin film by a voltage ranging from 10 kV to 200 kV. These high-energy ions penetrate the material over a typical length of a few dozen to a few hundred nanometers. In this way, ions dope, create defects, or even etch the material, depending on the fluence.

When the ions enter the target, they displace atoms from their original crystallographic positions, which may displace others in succession. As a result, the ion beam creates defects along the trajectories of the implanted ions. In this work, we use the implantation technique to introduce disorder along the incident ion paths and locally destroy the superconducting properties of $YBa_2Cu_3O_{7-\delta}$. The *d*-wave symmetry of the superconducting order parameter in $YBa_2Cu_3O_{7-\delta}$ makes it extremely sensitive to defects. Each defect acts as a depairing center for Cooper pairs. By controlling the amount of disorder introduced, the superconducting properties of a $YBa_2Cu_3O_{7-\delta}$ thin film can be finely tuned. The density of disorder can be quantified by the fraction of atoms in the crystal that have been displaced from their original sites, namely the displacement per atom (DPA). Lesueur *et al.* [50] have shown that it is possible to strongly decrease the T_c of $YBa_2Cu_3O_{7-\delta}$ for low values of DPA. A model based on the Abrikosov-Gor'kov pair-breaking mechanism allows us to account for this observation. Similar to the effect of magnetic impurities breaking Cooper pairs due to spin scattering in an *s*-wave superconductor, in a *d*-wave superconductor, when a Cooper pair scatters on a nonmagnetic crystal impurity, the initial wave vector is deflected in another direction, with a π phase shift. The Cooper pair is destroyed, which means that T_c is decreased. Following the approach of Abrikosov and Gor'kov, Lesueur *et al.* considered a finite lifetime for the Cooper pairs, which gives the reduction of T_c as a function of DPA:

$$\ln\frac{T_c}{T_{ci}} = \Psi\left(\frac{1}{2}\right) - \Psi\left(\frac{1}{2} + 0.14\frac{D}{D_c}\frac{T_{ci}}{T_c}\right), \qquad (1)$$

where T_{ci} is the initial critical temperature of the thin film before implantation and Ψ is the digamma function. Beyond the critical DPA, where T_c goes to zero, the material is a disordered metal, which progressively enters a localization regime as DPA is increased. At large DPA, the system undergoes a metal-to-insulator Anderson transition [66]. This is the property we are going to use in this work. Parts of the original thin film that are highly irradiated will be made insulating. This allows us to "print" superconducting circuits embedded in an insulating material, namely highly disordered HTSs.

The implantation technique in $YBa_2Cu_3O_{7-\delta}$ has been initially developed successfully to fabricate Josephson junctions [64,67–75]. Here, we use the ion-irradiation technique to shape $YBa_2Cu_3O_{7-\delta}$ thin films into 100-nm-wide wires.

B. Simulation methods

The ion beam creates defects all along the implanted ion trajectories. The control of the T_c of the film depends finely on the amount of disorder locally introduced in the thin film. This is directly related to the type of ions, their energy, and the dose.

Using Monte Carlo numerical simulations via the "Stopping and Range of Ions in Matter" (SRIM) software [76], it is possible to determine the appropriate range of parameters to control the superconducting properties of the irradiated film. This tool allows us to estimate the interaction zone of the implanted ions and the resulting defect rate created. We have performed simulations for two different types of ions of interest for $YBa_2Cu_3O_{7-\delta}$ devices, namely, O^+ and He^+ ions. Oxygen ions have the advantage of being one of the atoms in $YBa_2Cu_3O_{7-\delta}$ crystal structure, unlike Ga^{3+}, which can damage the superconducting properties through chemical substitution [60]. Helium atoms, on the other hand, can be focused into the thin film using the FIB technique, and remain light chemically neutral atoms for the material.

To perform a simulation, the density and chemical composition of the target must be defined layer by layer, as well as the incident ion and its energy. Using SRIM, one then obtains the trajectories of the ions in the material, which lose their energy by interacting with the electrons and colliding with the nuclei of the target. At each collision, the ion transfers some of its energy to the atom.

Each atom has its own displacement energy, which represents the minimum amount of energy required to move it out of its site, assuming that it will not fall back to its original position. If the energy transfer is greater than the displacement energy of the impacted atom, it is pushed out of its position, creating a vacancy in the crystal structure. The expelled atom will then produce a new collision sequence, colliding with other target nuclei, while the ion will follow its own collision sequence. Overall, the collision events create a collision cascade. The cascade stops when the ion and all ejected atoms have transferred their energy to phonons and electrons in the target. As a result, an ion creates many vacancies along its path. The vacancies can be filled by subsequent ejected atoms if they are of the same type. This is a replacement event, which does not contribute as a defect. As we are interested in a statistical evaluation, the collision cascade is calculated for large numbers of ions, typically 10^5 ions.

The SRIM simulation provides all the properties concerning the spatial distribution of defects. Figure 1 shows the generated DPA for the two different ion sources with an energy of 30 keV. The doses have been set so that the maximum DPA is similar for both types of ion. The first feature to be observed is the lateral extension of the disorder for a given DPA, shown in Fig. 1(a). The DPA generated by the simulation for He^+ ions has the shape of a sharp peak and decreases by 99% within a lateral extension of 5 nm, while for the O^+ case, this same extension reaches 40 nm. He^+ ions, which are much lighter than O^+ ions, travel further from the impact point and consequently create defects deeper in the layers. The last collision event occurs at a lateral extension of 280 nm for He^+ ions, whereas it stops at about 100 nm for O^+ ions. The same trend can be seen for the depth, when looking at Fig. 1(b): O^+ ions are stopped faster in the target compared to He^+ ions. At such an energy, the penetration depth of O^+ ions is about 100 nm, while it reaches more than 300 nm with He^+ ions. In view of this information, the He FIB has the potential to achieve a more accurate pattern with sharp edges using He^+ ions rather than O^+ ions. However, one must keep in mind that defects can be implanted far from the impact point. In the following, we will only focus on the realization of nanostructures using oxygen-ion implantation combined with electronic lithography.

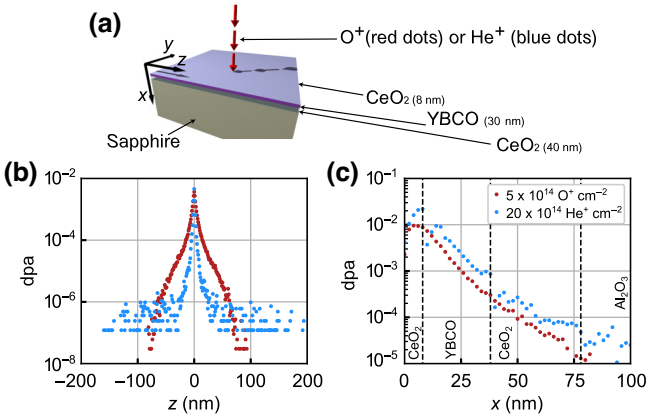

FIG. 1. The simulation of the DPA generated by a ponctual source of He^+ and O^+ ions with an energy of 30 keV into a stack of CeO_2 (8 nm)/$YBa_2Cu_3O_{7-\delta}$ (30 nm)/CeO_2 (40 nm)/Al_2O_3 (10^5 ions simulation). (a) The scheme of the irradiated sample, with the axes (x, y, and z), the different layers, and their thicknesses. Note that the scales are not respected. (b) The DPA averaged along the depth x in the $YBa_2Cu_3O_{7-\delta}$ layer at $y = 0$ as a function of the lateral dimension z. (c) The DPA at $y = 0$ and $z = 0$ as a function of the depth x. The dose is adjusted such that the maximum DPA values in (a) are equal for the He^+ ions and the O^+ ions. The black dashed lines separate the different material layers.

C. Ion-irradiation technique

Using the effect of ion implantation on the HTS superconductor, it is possible to engineer it at the nanoscale. To this end, we mask part of the sample with either a layer of gold or a layer of resist to protect it from exposure to the incident ion beam. The exposed part then has a lower T_c and can even become insulating depending on the DPA, while in the protected part, the superconducting properties remain intact. The use of SRIM numerical simulations is a valuable aid in selecting the appropriate thickness of the protective layer and also in determining the critical temperature profiles of the ion-irradiated area.

A protective layer is effective if the last defects occur before reaching the $YBa_2Cu_3O_{7-\delta}$ layer. As a heavy metal such as gold, with a density $d_{Au} = 19.3$ g cm^{-3}, is used, the gold layer stops the ions more effectively than the ma-N 2405 [77] resist layer, which has a density $d_{ma\text{-}N} = 0.95$ g cm^{-3}. We have determined the penetration depth of the ma-N2405 resist and gold layers when irradiated with 30-keV oxygen ions and found 250-nm and 100-nm depths, respectively. By choosing a layer thickness greater than the penetration depth, we ensure that the ions do not penetrate the $YBa_2Cu_3O_{7-\delta}$ superconducting layer regardless of the chosen dose. During fabrication, we therefore set a gold-layer thickness greater than 150 nm and a ma-N2405 resist layer thickness greater than 300 nm as a minimum.

Further interesting information from the numerical simulation is the possibility of estimating the T_c profile of an irradiated protected area. Figure 2 represents the T_c reduction profile created by 30 keV O^+ irradiation through a 100-nm-wide resist mask patterned on a 30-nm $YBa_2Cu_3O_{7-\delta}$ thin film and protected by an 8-nm-thick CeO_2 layer. The heat map in Fig. 2(b) shows the reduction of T_c in the x-z plane by converting the DPA using Eq. (1). The white outline shows the edges of the wire, which correspond to $T = 0$ K. They are curved because

the ions introduce different amounts of disorder at different depths into an overall shape described as the "interaction pear." By examining, in Fig. 2(b), the different cross sections along the z direction of the thermal map at different x depths, one can note that the T_c varies significantly but not abruptly. It is possible to evaluate the width of the wire at different depths for different temperatures, as shown in Fig. 2(c). It can be seen that the width decreases with the depth. Furthermore, as the temperature increases, the edges of the superconducting wire transit to the normal state and the width of the wire decreases accordingly, as shown in Fig. 2(d). Finally, Fig. 2(e) summarizes this information and shows that the average width decreases slowly until half of T_c and quickly becomes zero afterward. From our simulation, the width of the wire is reduced by 20 nm at low temperature compared to the 100-nm nominal width of the lithographic mask, thus adopting a tapered cross section. The dependence of T_c on x and z under the irradiation conditions can be extracted from the simulation. The numerical simulations thus make it possible to deduce a geometry for a fixed T_c criterion. Close to the wire walls, we have a T_c gradient, to which corresponds a critical current gradient. The lower the temperature, the greater is the width of the superconducting wire. The fine detail of the current flow can therefore be deduced.

In the following, we describe the different steps in the implementation of this irradiation technique to fabricate nanowires.

D. Device fabrication

The nanofabrication process involves several steps, performed in a cleanroom. We have succeeded in developing a reproducible, robust, and versatile method to fabricate $YBa_2Cu_3O_{7-\delta}$ nanostructures using laser lithography, electron-beam lithography, and ion irradiation. These methods are not specific to SNSPDs but can also be applied to any other type of $YBa_2Cu_3O_{7-\delta}$-based device for a variety of applications.

To avoid degradation of $YBa_2Cu_3O_{7-\delta}$ by direct exposure to the atmosphere, we have developed, in collaboration with Ceraco and the Unité Mixte de Physique CNRS–Thales (UMPhy), a method of growing thin films to keep them fully protected by a layer impermeable to oxygen diffusion, while maintaining ohmic contact with the $YBa_2Cu_3O_{7-\delta}$ by depositing a gold layer *in situ* after growth.

The special method of manufacturing the thin film consists of a 5-mm-diameter 8-nm-thick disk of CeO_2 protecting the central area of the $YBa_2Cu_3O_{7-\delta}$ thin film, while the entire area is covered on top by a 20-nm-thick layer of Au. After standard coevaporation or pulsed-laser deposition performed with the usual deposition parameters for $YBa_2Cu_3O_{7-\delta}$ (at high temperature and under an oxygen atmosphere), the sample is lowered in temperature to

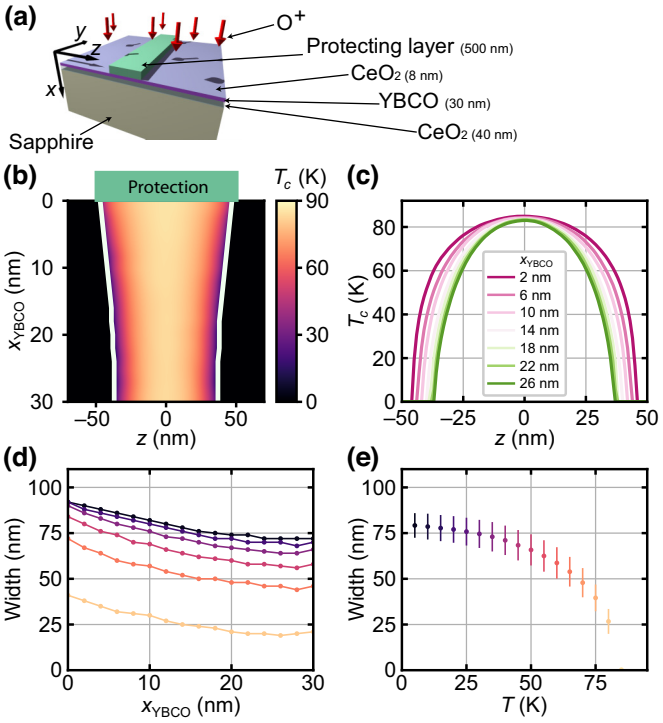

FIG. 2. The simulation of 30-keV O^+ irradiation in a sample of a 30-nm-thick $YBa_2Cu_3O_{7-\delta}$ thin film, protected by a 100-nm-wide and 500-nm-thick ma-N2405 resist for an ion dose of $D = 5 \times 10^{14}$ ions cm^{-2}. The DPA are converted to T_c using Eq. (1) for better understanding. (a) The scheme of the irradiated sample, where the axes (x, y, and z), the different layers, and their thicknesses are indicated. Note that the scales are not respected. (b) A heat-map plot of T_c in the x-z plane of the $YBa_2Cu_3O_{7-\delta}$ layer. The white contour corresponds to $T_c = 0K$. (c) The lateral variation of T_c at different depths x. (d) Variation of the wire width for different depths and temperatures, taken from (b). (e) The evolution of the width of the wire as a function of the temperature. The color scales in (d) and (e) are the same as the color bar in (b).

50°C under an oxygen atmosphere and the CeO_2 layer is deposited as follows. At room temperature and pressure, a mechanical mask is aligned on the sample to deposit the CeO_2 capping layer only in the center of the sample. Deposition takes place at 650°C in an oxygen atmosphere; then the sample is cooled to 50°C in an oxygen atmosphere. The shading mask is removed at room temperature and pressure. The sample is again heated to 650°C and then cooled to 50°C under an oxygen atmosphere to ensure optimum oxygen doping of the $YBa_2Cu_3O_{7-\delta}$ layer not covered with CeO_2, after which 20 nm of *in situ* gold is deposited over the entire sample surface. By following these steps, we ensure that the films are optimally oxygen doped. The thin insulating protective layer of CeO_2 has several advantages. This material is stoichiometric during the deposition and very stable, avoiding any change in the stoichiometry of

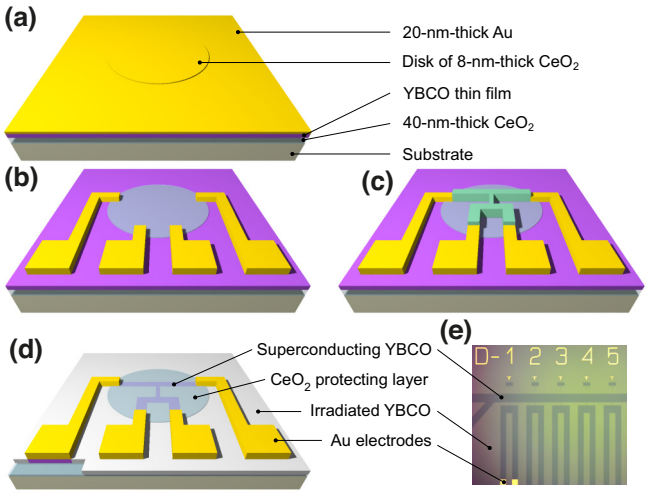

FIG. 3. (a)–(d) The fabrication work flow described in the text.

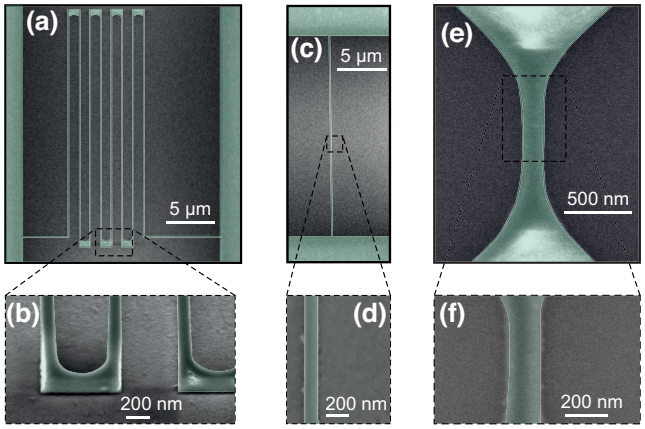

FIG. 4. SEM pictures of different devices on 30-nm-thick $YBa_2Cu_3O_{7-\delta}$ protected by a 8-nm-thick CeO_2 capping layer. The visible part is the resist layer, which protects against ionic irradiation. (a) The meander geometry of a long nanowire with dimensions 450 μm × 500 nm. (b) A tilted view on one part of the meander shown in (a). (c) A nanowire with dimensions 150 nm × 20 μm. (d) An enlargement of one part of the long wire shown in (c). (e) A short nanowire with dimensions 200 nm × 500 nm. (f) An enlargement of one part of the short wire shown in (e).

the $YBa_2Cu_3O_{7-\delta}$. Furthermore, it is already used as a 40-nm-thick buffer layer on sapphire substrates to allow the growth of $YBa_2Cu_3O_{7-\delta}$. With this technique, we have obtained good electrical contacts outside the disk area, while the central area is still protected by the blue CeO_2 disk shown in Fig. 3.

The first step is lithography to design the electrodes with dimensions larger than 10 μm. After depositing a 500-nm-thick layer of S1805 photoresist baked at 110°C, we pattern it with a PhotonSteer LW450C laser-lithography system. During this step, the exposed areas will be developed and will define the gold layer of the contact electrodes. These gold electrodes are designed to reach the superconducting central part of the sample protected by the CeO_2 layer, thus ensuring excellent electrical contact. Once the sample is developed, we deposit a 0.5-nm-thick Ti layer as an adhesion layer, followed by a 200-nm-thick Au layer in a Plassys SEM 550S thin-film evaporation. After this step, we perform a lift-off, followed by an argon-ion etch of the whole sample for 1 min, thus allowing us to define the contacts as shown in Fig. 3(b).

The second step consists in making the superconducting electrodes and nanowires protected by the CeO_2 and not covered with Au. We cover the sample with a 500-nm-thick ma-N2405 electroresist baked at 90°C. Then, we perform the mask exposure in two successive steps of electron lithography using the FEI ThermoFisher Magellan 400 electron microscope: the finest details, in the order of 100 nm, are performed at low current (11 pA) and ultra-high resolution, while the larger patterns are performed at high current (26 nA) and standard resolution. After development, we have the sample shown in Fig. 3(c). Figure 4 is an electron-microscope image of the different types of wire geometry present on each of the chips. There are wires ranging in width from 100 nm to 5 μm and in length from 500 nm to 500 μm, for a film thicknesses of 30 nm in this work. Note that the SEM images in Figs. 4(a) and 4(c) seem to reinforce the crowding effect at the connection of the wire but the geometry has the same rounding as in Fig. 4(e). The third step, after development of the insulated sample, shown in Fig. 3(c), is dedicated to the ion-irradiation process illustrated in Fig. 2(a).

The irradiation was performed at the ICUBE laboratory in Strasbourg. The samples were carbon fixed to the center of a 3-in.-diameter metal target to thermalize the substrate and evacuate the charges during ion irradiation. The targets were then placed in the treatment chamber under a 10^{-6} mbar vacuum. The ions were expelled from the oxygen source and accelerated to an energy of 30 keV. The ion beam was scanned through a 3-in.-diameter diaphragm with a current of 6 μA, which corresponds to a current density of 132 nA cm^{-2} and a total dose of $D = 3 \times 10^{14}$ ions cm^{-2} for a 6 min 42 s irradiation time. The ion-beam scanning parameters (time, dose, and area scanned) ensure homogeneous irradiation of the 1 cm^2 sample surface.

The last step consists in removing the resist completely. Prior to the lift-off, we perform an O^+ plasma stripping with a Corial 200I ICP-RIE for 1 min. We thus obtain the devices schematized in Fig. 3(d). An optical image [Fig. 3(e)] shows a typical sample in which the superconducting nanowires and electrodes are fully encapsulated. One chip contains between 28 and 250 nanowires, depending on the EBL layout, with several widths, lengths, and geometries. Working with different types of starting layers,

we can compare the quality of the nanowires fabricated with our method. A distinction was made between the "N" samples, which are entirely covered with a layer of CeO_2, and the "CS" and "JS" samples, which are protected by an 8-nm-thick CeO_2 disk in the center of the chip and then covered with 20 nm of gold throughout. The "N" and "CS" samples were fabricated by Ceraco using a coevaporation technique and the "JS" ones were fabricated by Thales using a pulse-laser deposition technique, respectively. Note that for the fabrication of nanowires with a N-type sample, an additional contact-defining step is required, which includes argon-ion-beam etching of the top CeO_2 layer and *ex situ* deposition of the gold layer. We have verified by an *ad hoc* procedure on test samples that the etching process does not affect the $YBa_2Cu_3O_{7-\delta}$ layer. This leads to high contact resistance up to 100 kΩ.

E. Electrical characterization

The first step in the electrical characterization of the devices is to measure the resistance as a function of the temperature in a four-point geometry, to suppress the contribution of contact and wire resistance. To do this, the sample is bonded to a copper sample holder with silver paste to ensure proper thermalization. The gold electrodes of the relevant devices are wire bound to a printed circuit board (PCB). The sample holder is then attached to the base plate of an Optidry pulse-tube cryostat with thermal decoupling parts and is fitted with a calibrated resistor for temperature measurement and a heating resistor allowing temperature ramps from 4.5 K to 120 K at a rate of 2K min^{-1}, using a CryoCon 24C temperature controller. The PCB itself is connected inside the cryostat to 12 twisted pairs of manganese wires. These wires are low-pass filtered at the input of the cryostat and are thermalized at each stage of the cryostat, limiting thermal noise and heat transfer. To measure the resistance versus the temperature, we use a Yokogawa GS200 dc current source and a Keithley 2400 voltage multimeter. We apply a dc current $I_{dc} = 100$ nA through the device and reverse the polarity every second. At the same time, the voltage is measured alternately for each of the currents. This allows us to extract the voltage drop across the device by removing the voltage offset.

The second characterization step for evaluating the quality of the devices is the measurement of the current-voltage (I-V) characteristics. At a fixed temperature, the current I is incremented by one current step δI every 100 ms and we measure the corresponding voltage drop V.

Figure 5 shows typical resistivity versus temperature curves for different wire sizes (the lengths and widths are specified in the inset to Fig. 5) in linear scale [Fig. 5(a)] and logarithmic scale [Fig. 5(b)] on a 30-nm-thick CS film. The resistivity shows a wider transition as the wire width decreases [Fig. 5(a)]. Furthermore, the resistivity in

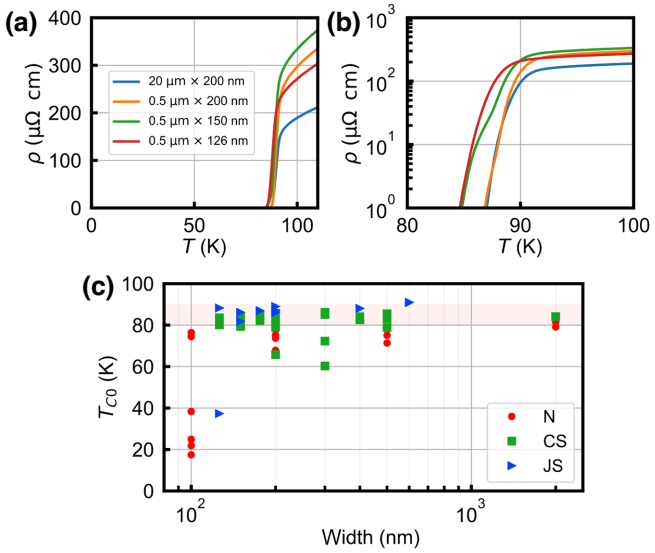

FIG. 5. The temperature evolution of the resistivity of superconducting nanowires patterned on 30-nm-thick $YBa_2Cu_3O_{7-\delta}$ film, in (a) linear and (b) logarithmic scales, respectively. (c) The evolution of the critical temperature at zero resistance T_{c0} with respect to the width for nanowires patterned on 30-nm-thick samples of different types.

logarithmic scale [Fig. 5(b)] allows us to visualize more clearly the presence of a foot in the transition. Figure 5(c) shows the zero-resistivity temperatures T_{c_0} as a function of the width of the wires, made on different types of samples. We note a large dispersion of data points for N-type samples. The superconducting properties change significantly from one device to another. Moreover, T_{c_0} is often greatly reduced down to 20 K when approaching the 100-nm width limit. Note that many devices in the N-type samples could not be measured correctly due to the high contact resistance resulting from the contact-making step described above. This led us to make a new generation of samples: the CS-type samples. The new protection method implemented in the CS samples ensures ohmic contact resistances between the $YBa_2Cu_3O_{7-\delta}$ and gold layers, due to the fact that the latter is deposited *in situ*, just after the CeO_2 protective layer.

Although T_{c_0} dispersion also exists for CS samples, it does not extend beyond a dozen kelvin across all widths. If we look more specifically at the narrowest superconducting wires, these have an average T_{c_0} lowered by just a few kelvin compared with devices that are 2 μm wide. While dispersion in T_{c_0} also exists for CS samples, it only extends over a range of 10 K. Furthermore, this broadening does not occur systematically at the narrowest width of the nanowire. This makes the technique more reliable when using CS-type samples rather than N-type ones. We also point out that the narrowest superconducting wires

have a T_{c_0} lowered by only a few kelvin compared to the 2-μm-wide devices.

Most CS nanowires have a T_{c_0} higher than 80 K. This statistic comes from the measurement of three different CS chips (more than 200 devices), from two different batches, which shows that these results are very reproducible. We will see that this trend is also present in the measurements of the *I-V* characteristics. In addition, the superconducting properties are additionally preserved for several tens of months—the last samples measured were characterized 28 months after their manufacture. These observations are strong arguments demonstrating the robustness of $YBa_2Cu_3O_{7-\delta}$ films to oxygen diffusion and ageing. Here, we have thus validated the control, reproducibility, and durability of high-quality nanowires made by oxygen-ion irradiation from 30-nm-thick $YBa_2Cu_3O_{7-\delta}$ thin films protected by a CeO_2 disk. Regarding the fabrication of nanowires from 30-nm-thick JS type samples, the quality of the devices has improved significantly. As we can see from the figures, the devices compete with the best devices obtained on CS-type samples in terms of T_{c_0}: overall, they have a T_c that is higher by a few kelvin.

After these first measurements, we examine the *I-V* characteristics. The current-voltage (*I-V*) curve provides valuable information on the behavior and single-photon-detection potential of superconducting nanowires. Regardless of the device geometry, the nanowire current density j is computed with respect to its superconducting cross section $A = wd$ as $j = I/(wd)$. The width w and the length l are estimated from the electron-beam lithography with a precision of about a few percent to dozens of percent for the narrowest wire, which is, in any case, overestimated regarding the irradiation profile described above.

In Figs. 6(b) and 6(c), we show two typical voltage characteristics of current density (*j-V*) at 10 K, measured for increasing and decreasing scans of two different wires of length 500 nm and width 300 nm. We extract the critical current density j_c as the value of the current for a voltage of 5 μV that is greater than the voltage noise [see the inset of Fig. 6(b)]. The (*j-V*) curves can show very different behaviors, which can be classified into two categories depending on the value of j_c. This criterion has been also reported in other type of $YBa_2Cu_3O_{7-\delta}$ nanowires [38]. For values of j_c lower than an experimental criterion of $j_{h0} = 5 - 10 \times 10^6$ A cm^{-2}, the voltage increases continuously until it reaches the ohmic state. The upward- and downward-sweep curves merge completely [Fig. 6(c)]. This behavior is consistent with the flux flow regime. When j_c is greater than j_{h0}, a metastable state appears, the signature of which is a hysteretic *j-V* characteristic due to the Joule effect in the normal state competing with the cooling of the electrons. For V < 1 mV, the wire exhibits a flux flow regime that results in a rapid increase in voltage while the current varies slowly [see the inset of Fig. 6(b)]. As the current increases further, a sudden high-voltage switching occurs, greater than 1 V [Fig. 6(b)]. The corresponding current density and voltage are the switching current density j_s, indicated in the inset of Fig. 6(b), and the switching voltage V_s, respectively.

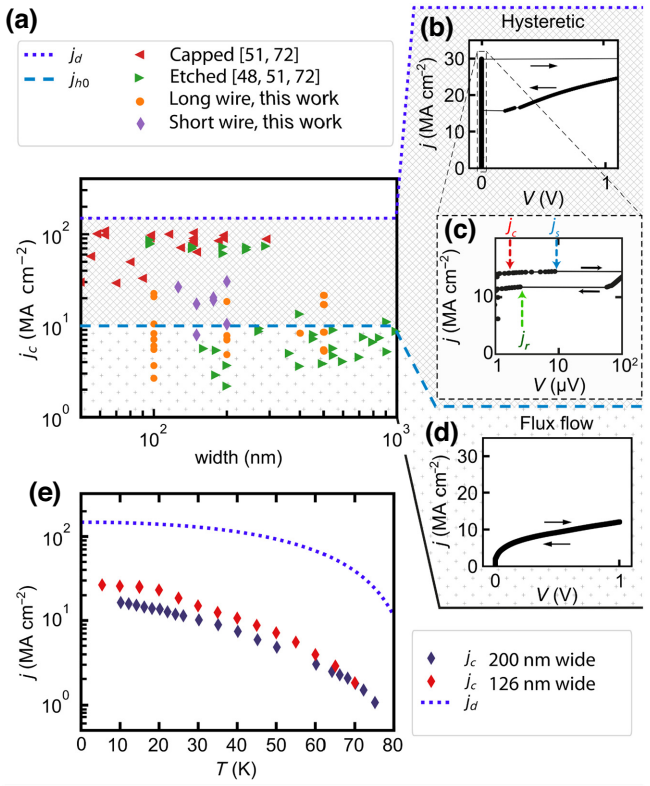

FIG. 6. (a) The evolution of the critical current j_c at 10 K as a function of the nanowire width. (b)–(d) Depending on the j_c value, the nanowires belong to two categories: if $j_c > j_{h0}$, the *I-V* curve is hysteretic as represented in (b) while for $j_c < j_{h0}$, the *I-V* curve has a flux flow behavior as shown in (d). The orange circle and purple diamond represent the critical current densities for short and long wires, respectively, made here, and the red and green triangles are, respectively, the critical current densities for protected and unprotected wires made using other techniques [51,55,78]. (c) The hysteretic *I-V* curve in log-log scale, with an enlargement around 0 V. The switching current j_s (red arrow), the returning current j_r (green arrow), and the critical current j_c (blue arrow) are indicated. (e) A typical evolution of the critical current j_c as a function of the temperature for two short nanowires of width 200 nm and 126 nm.

III. DISCUSSION

Figure 6(a) summarizes the data from all the devices fabricated in this work, along with data collected from other work where the devices were made using other techniques [51,55,78]. The theoretical Ginzburg-Landau depairing-current density [79] j_d, expressed as $j_d(t) = \Phi_0/(3\sqrt{3}\pi\mu_0\lambda_L(T)^2\xi(T))$, where Φ_0 is the magnetic flux quantum, $\xi_0 = 2$ nm, and $\lambda_L(0) = 180$ nm for $YBa_2Cu_3O_{7-\delta}$, is added to the plot, at 10 K in Fig. 6(a) and

as a function of temperature in Fig. 6(e). Regardless of the fabrication technique, the critical current density defines to which categories the device belongs. Note that all j_c are below the theoretical depairing-current density j_d marked by the short-dotted line but approach it.

Encapsulated wires fabricated using our ion-irradiation technique (orange round dots for the short 500-nm wires and purple diamonds for the long 20-μm wires) exhibit high voltage jumps, up to 1 V amplitude at 10 K. In addition, they can be used directly in the state for single-photon detection, since there is no opaque layer protecting them from visible radiation. Furthermore, they remain stable under thermal cycling, over time and under storage conditions in a dry ambient environment. The remarkable data of the other works (red triangles) have been obtained in the presence of a gold layer, which when removed, degrades the wires considerably. The vast majority of the wires no longer exhibit hysteresis.

For single-photon detection, we are looking for hysteretic behavior, which is the signature of a thermal runaway favorable to single-photon detection. Figure 7(b) shows the I-V curves for different temperatures, demonstrating an increasing switching voltage as the temperature is lowered.

Using the model developed by Skocpol, Beasley, and Tinkham (SBT) [80], we can account for the critical current density threshold necessary to observe the hysteresis. Such a description has widely been used to model the self-heating of superconducting nanowires at low [81–83] and high [28,84] critical temperatures.

In the original paper, SBT studied the heat transfer in a one-dimensional wire of thickness d, width w, and length l. In Fig. 7(a), a schematic of such a biased nanowire under a current I is presented: a hot normal region of length $2 \times y_0$ is at the center of the bridge. Depending on the thermal properties and dimensions of the wire, the normal region is maintained by the Joule effect or dissipated by both heat transfer through the superconducting thin film and the substrate. The temperature evolution $T(y)$ along the bridge is written as

$$-\kappa_n \frac{d^2T}{dy^2} + \frac{\alpha}{d}(T - T_b) = \left(\frac{I}{wd}\right)^2 \rho \quad (y < y_0), \tag{2a}$$

$$-\kappa_s \frac{d^2T}{dy^2} + \frac{\alpha}{d}(T - T_b) = 0 \quad (y > y_0), \tag{2b}$$

where κ_n and κ_s are the thermal conductivity in the normal and the superconducting states, respectively, ρ is the film resistivity, T_b is the bath temperature, and α is the thermal conductance per unit area. For the normal region, the right-hand term of Eq. (2a) is Joule heating. On the left-hand side of Eq. (2a), the first term corresponds to the thermal conduction of the nanowire in the normal and superconducting phase, respectively, while the second term represents the thermal transfers through the substrate. As a first approach, assuming that the conductivities are identical, i.e., $\kappa = \kappa_s = \kappa_n$, the equilibrium between these terms naturally leads to a characteristic thermal length η_h, called the healing length and expressed as

$$\eta_h = \sqrt{\frac{\kappa d}{\alpha}}. \tag{3}$$

Depending on the length l of the nanowire compared with the healing length η_h, there are two types of behavior: either, for $l > \eta_h$, heat is dissipated mainly through the substrate, preventing the hot spot from extending across the entire width of the nanowire, which remains in the superconducting state; or, for $l < \eta_h$, heat exchange within

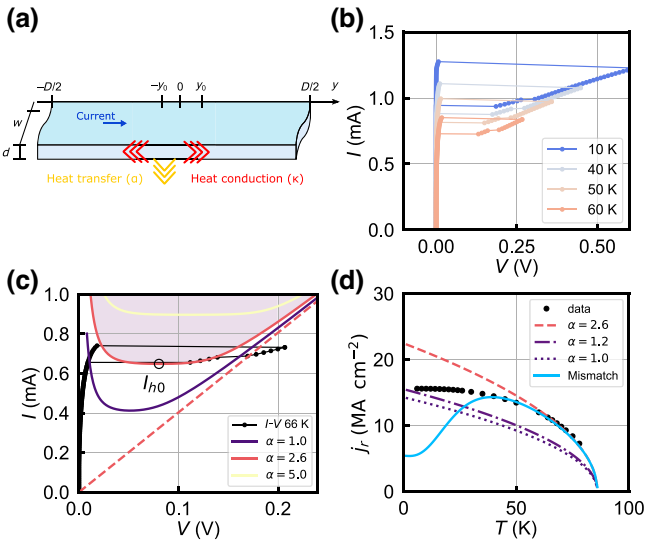

FIG. 7. (a) The schematics of a biased current wire in the framework of the SBT thermal model. A normal hot region of length $2y_0$ along the y axis (in red) transfers thermal energy laterally to the superconducting wire via heat conduction κ and through the substrate due to the heat transfer α. Depending on the values of α and κ, the hot region either expands or self-heals. (b) I-V curves measured at different temperatures for C8, a 30-nm-thick 500-nm-long 200-nm-wide $YBa_2Cu_3O_{7-\delta}$ nanowire. (c) The SBT self-heating model in linear scale with a C8 I-V curve at 66 K. The solid lines are simulations of the I_hV_h parametric curves given by Eqs. (4) and (5). We set different values of α, displayed in the legend in units of 10^7 W K^{-1} m^{-2}, with $\kappa = 1.6$ W K^{-1} m^{-1}. The pink area defines the zone in which the device is thermally unstable for $\alpha = 2.6 \times 10^7$ W K^{-1} m^{-2}. The corresponding minimum healing current j_{h0} is highlighted by the black circle. The dashed line is the asymptotic line of the ohmic state in the SBT simulation. (d) The temperature evolution of the returning current density for C8. The lines correspond to the simulations of the healing-current density j_{h0} for different values of the surface heat transfer α (in units of 10^7 W K^{-1} m^{-2}) and for a temperature-dependent $\alpha(T)$ using the phonon mismatch model ("Mismatch" in the key).

the superconducting nanowire dominates and the hot spot propagates throughout the nanowire. The result is a superconducting transition to the normal state, the signature of which is both hysteresis and switching in the *I-V* curves.

To estimate η_h in our $YBa_2Cu_3O_{7-\delta}$ nanowires on sapphire substrate, we use $\alpha \approx 1 \times 10^7$ W K^{-1} m^{-2} [85] and $\kappa_n \approx 0.8 - 3$ W K^{-1} m^{-1} [86].

Using these two limiting values for thermal conductivity, the healing length of a 30-nm-thick $YBa_2Cu_3O_{7-\delta}$ film can be estimated to be $\eta_h \approx 50 - 100$ nm.

In our case, the nanowires are always longer than the estimated healing length, while their width is of the same order of magnitude or greater than the healing length. For long bridges $l \gg \eta_h$, assuming that the temperatures at its ends are equal to the bath temperature and that T and $\kappa(dT/dy)$ are continuous at the normal-superconductor interface, the current flow required to maintain a static hot spot is written as [80]

$$I_h(y_0) = \sqrt{\frac{\alpha w^2 d(T_c - T_b)}{\rho}} \times \sqrt{\left[1 + \left(\frac{\kappa_s}{\kappa_n}\right) \coth\left(\frac{y_0}{\eta_N}\right) \coth\left(\frac{L}{2\eta_S} - \frac{y_0}{\eta_S}\right)\right]}. \tag{4}$$

Using Ohm's law, the corresponding voltage drop along the wire is written as

$$V_h(y_0) = \frac{2y_0 \rho I_h(y_0)}{wd}. \tag{5}$$

The parametric healing curves I_hV_h of Eqs. (4) and (5) depend on the thermal properties and dimensions of the superconducting nanowire. In Fig. 7(c), we have plotted both the healing curves from the simulation for three values of surface heat transfer α as well as the measured hysteretic *I-V* curve at 66 K of a nanowire of thickness 30 nm, length 500 nm, and width 200 nm.

Note that the minimum point I_{h_0} of the curve I_hV_h is the highest current value for which the hot spot heals. Thus, in the *I-V* return curve, I_{h_0} is equal to the value of the return current I_r that returns the nanowire to the superconducting state.

Using a resistivity of $\rho(100\,\text{K}) = 300$ μΩ cm and a critical temperature of $T_{c0} = 86.1$ K for our nanowire, we were able to simulate the I_hV_h by adjusting the surface heat-transfer coefficient α and the thermal conductivity κ so that the simulated curve intersects the returning and switching data points. We found $\alpha = 2.6 \times 10^7$ W K^{-1} m^{-2}, $\kappa = \kappa_s = \kappa_n = 1.6$ W K^{-1} m^{-1} and obtained the following healing-current density: $j_{h0} \approx 11$ MA cm^{-2}. Here, the values of α and κ estimated from the simulation are consistent with those reported [85,86].

We now examine the evolution of the return-current density j_r as a function of temperature as well as the thermal SBT simulation of the healing-current density j_{h_0} for different constant values of the surface-heat-transfer coefficient as shown in Fig. 7(d). For the value $\alpha = 1.0$ [85], the simulation underestimates the healing-current density j_{h_0}, while the case $\alpha = 1.2$ corresponds to the value of j_{h_0} at high and low temperature but the overall shape of j_r with regard to the temperature is not reproduced. Finally, the model for $\alpha = 2.6$ corresponds to the global experimental evolution of j_r from high temperature down to 66 K but overestimates it at low temperature. Moreover, such a heat-transfer value is almost 3 times higher than that reported in the literature [85].

We can refine the SBT model by including the temperature dependence of the thermal conductance α. Taking into account that the phonon wavelength increases with decreasing temperature, this results in a shift of the acoustic wavelength at the interface for low temperatures [87,88] called acoustic mismatch, which leads to a reduction in surface heat exchange. The introduction of such an effect [86] in the SBT model is written as

$$\frac{1}{\alpha} = A + \frac{B}{T^3}. \tag{6}$$

With $A^{-1} = 2.61 \times 10^7$ W K^{-1} m^{-2} and $B = 9 \times 10^{-4}$ K^4 m^2 W^{-1} for our system, we can fit our data up to 35 K, as shown by the blue line in Fig. 7(d). Below 35 K, the model no longer accounts for the evolution of j_r with the temperature. We have therefore improved the reproduction of the experimental data down to 35 K.

Considering the validity domain of the SBT model, we can explain the deviation between the model and the data. We have not added the temperature dependence of κ but several works have reported an increase of κ around 40–50 K [89–91]. This should result in larger heat transfers in the superconducting state and therefore larger values of the return current j_r. Note that heat exchange with the substrate may be less efficient than within the superconducting nanowire, depending on the length $2 \times y_0$ of the hot spot, which can range from 1 nm to 250 nm. The increase in κ associated with the decrease in α for low temperatures leads to values of η_h greater than the wire width. This is outside the assumptions of the SBT model. We can thus understand that at low temperatures, our model cannot reproduce the experimental data.

IV. CONCLUSIONS

In conclusion, we have demonstrated a technique to produce high-temperature superconducting nanowires fabricated by ion irradiation combined with standard electron-lithography techniques. The nanowires are fully encapsulated in an environment that protects them from any form of degradation by oxygen migration or exposure during the

fabrication steps. The quality of the superconducting properties and their robustness over time illustrates the strength of this superconducting nanowire milling technique as a prime method for the development of scalable irradiated high-temperature superconducting nanowire single-photon detectors. We have shown that most of the nanowires produced using our technique have very high critical current densities, allowing hysteresis and a voltage jump in the order of 1 V. The understanding of such behavior up to 35 K in the framework of the SBT model allows us to highlight the conditions for the development of a hot spot, which is a prerequisite for obtaining a single-photon detector in high-critical-temperature superconducting nanowires. This condition may be not sufficient to make a SNSPD. In a Ginzburg-Landau–based calculation, Vodolazov [45] has shown that the ratio between the electron and phonon heat capacities is essential to estimate the values of the width of the nanowire and the critical current density, favorable to detect each absorbed photon (deterministic SNSPD). In the case of high-T_c materials, these numbers are $d = 10$ nm and $j_c \sim 0.9\, j_d$. While this calculation captures an essential part of the SNSPD functioning, and certainly points towards two important critical parameters, there is still uncertainties on the absolute values required. Ginzburg-Landau is a theory valid close to T_c, while the SNSPD are supposed to operate well below $T_c/2$. The quasiparticle excitation spectrum depends on the material and high-T_c superconductors are unconventional in this respect. Thin films may have different material parameters than the bulk—e.g., such as λ_L—that set j_d. Note that the controversial debate on the possibility of having a single-photon response seems to be dying out in view of the latest results obtained on ultrathin $Bi_2Sr_2CaCu_2O_{8+\delta}$ layers [39,40], which exhibit single-photon response but may be not in the deterministic regime. Our nanowires will be good candidates, provided that the properties of the starting film are further improved with a thickness further reduced to about 10 nm—in particular, to trap vortices and remove the dissipative part before the nanowire switches to its resistive state—and their width probably to below 100 nm [45]. This development is in progress and is beyond the scope of this work.

ACKNOWLEDGMENTS

We thank Yann Legall (ICube laboratory, Strasbourg) for the ion irradiation. This project has received funding from the European Union Horizon 2020 research and innovation program under the Marie Skłodowska-Curie Grant Agreement No. 754387. This work has been supported by the Agence nationale de la recherche (ANR) "Jeunes chercheuses et jeunes chercheurs" (JCJC) program (HECTOR ANR-21-CE47-0002-01), by Thales through a Co-fund Ph.D. fellowship, by Region Ile-de-France in the framework of the Domaine de recherche et d'Innovation Majeur (DIM) Quantum Technologies in Paris Region (QuanTiP) program and the DIM Nano-K and Sesame programs, and by the French RENATECH network (the French national nanofabrication platform).

[1] A. McCarthy, N. J. Krichel, N. R. Gemmell, X. Ren, M. G. Tanner, S. N. Dorenbos, V. Zwiller, R. H. Hadfield, and G. S. Buller, Kilometer-range, high resolution depth imaging via 1560 nm wavelength single-photon detection, Opt. Express **21**, 8904 (2013), ISSN 1094-4087.

[2] Z. Zhang, C. Chen, Q. Zhuang, J. E. Heyes, F. N. C. Wong, and J. H. Shapiro, in *Conference on Lasers and Electro-Optics*, page FTu3G.5 (San Jose, California, 2018). OSA. ISBN 978-1-943580-42-2.

[3] H.-L. Yin, T.-Y. Chen, Z.-W. Yu, H. Liu, L.-X. You, Y.-H. Zhou, S.-J. Chen, Y. Mao, M.-Q. Huang, W.-J. Zhang, H. Chen, M. J. Li, D. Nolan, F. Zhou, X. Jiang, Z. Wang, Q. Zhang, X.-B. Wang, and J.-W. Pan, Measurement-device-independent quantum key distribution over a 404 km optical fiber, Phys. Rev. Lett. **117**, 190501 (2016), ISSN 0031-9007, 1079-7114.

[4] A. V. Glejm, A. A. Anisimov, L. N. Asnis, Yu. B. Vakhtomin, A. V. Divochiy, V. I. Egorov, V. V. Kovalyuk, A. A. Korneev, S. M. Kynev, Yu. V. Nazarov, R. V. Ozhegov, A. V. Rupasov, K. V. Smirnov, M. A. Smirnov, G. N. Goltsman, and S. A. Kozlov, Quantum key distribution in an optical fiber at distances of up to 200 km and a bit rate of 180 bit/s, Bull. Russ. Acad. Sci.: Phys. **78**, 171 (2014), ISSN 1062-8738, 1934-9432.

[5] J. Yin *et al.*, Satellite-based entanglement distribution over 1200 kilometers, Science **356**, 1140 (2017), ISSN 0036-8075, 1095-9203.

[6] L. Xue, Z. Li, L. Zhang, D. Zhai, Y. Li, S. Zhang, M. Li, L. Kang, J. Chen, P. Wu, and Y. Xiong, Satellite laser ranging using superconducting nanowire single-photon detectors at 1064 nm wavelength, Opt. Lett. **41**, 3848 (2016), ISSN 0146-9592, 1539-4794.

[7] D. M. Boroson, B. S. Robinson, D. V. Murphy, D. A. Burianek, F. Khatri, J. M. Kovalik, Z. Sodnik, and D. M. Cornwell, in *SPIE LASE*, edited by Hamid Hemmati and Don M. Boroson (San Francisco, California, 2014), p. 89710S.

[8] C. M. Natarajan, L. Zhang, H. Coldenstrodt-Ronge, G. Donati, S. N. Dorenbos, V. Zwiller, I. A. Walmsley, and R. H. Hadfield, Quantum detector tomography of a time-multiplexed superconducting nanowire single-photon detector at telecom wavelengths, Opt. Express **21**, 893 (2013), ISSN 1094-4087.

[9] L. K. Shalm *et al.*, Strong loophole-free test of local realism, Phys. Rev. Lett. **115**, 250402 (2015), ISSN 0031-9007, 1079-7114.

[10] R. Riedinger, S. Hong, R. A. Norte, J. A. Slater, J. Shang, A. G. Krause, V. Anant, M. Aspelmeyer, and S. Gröblacher, Non-classical correlations between single photons and phonons from a mechanical oscillator, Nature **530**, 313 (2016), ISSN 0028-0836, 1476-4687.

[11] www.princetonlightwave.com. (2022).

[12] G. N. Gol'tsman, O. Okunev, G. Chulkova, A. Lipatov, A. Semenov, K. Smirnov, B. Voronov, A. Dzardanov, C.

Williams, and R. Sobolewski, Picosecond superconducting single-photon optical detector, Appl. Phys. Lett. **79**, 705 (2001), ISSN 0003-6951, 1077-3118.

[13] C. M. Natarajan, M. G. Tanner, and R. H. Hadfield, Superconducting nanowire single-photon detectors: Physics and applications, Supercond. Sci. Technol. **25**, 063001 (2012), ISSN 0953-2048, 1361-6668.

[14] E. A. Dauler, M. E. Grein, A. J. Kerman, F. Marsili, S. Miki, S. W. Nam, M. D. Shaw, H. Terai, V. B. Verma, and T. Yamashita, Review of superconducting nanowire single-photon detector system design options and demonstrated performance, Opt. Eng. **53**, 081907 (2014), ISSN 0091-3286, 1560-2303.

[15] R. H. Hadfield, Single-photon detectors for optical quantum information applications, Nat. Photonics **3**, 696 (2009), ISSN 1749-4885, 1749-4893.

[16] http://www.scontel.ru, https://www.idquantique.com/, https://singlequantum.com/, https://www.qdusa.com/, and http://www.sconphoton.com. (2022).

[17] K. Smirnov, A. Divochiy, Y. Vakhtomin, P. Morozov, P. Zolotov, A. Antipov, and V. Seleznev, NbN single-photon detectors with saturated dependence of quantum efficiency, Supercond. Sci. Technol. **31**, 035011 (2018), ISSN 0953-2048, 1361-6668.

[18] F. Marsili, Detecting single infrared photons with 93% system efficiency, Nat. Photonics **7**, 5 (2013).

[19] A. Vetter, S. Ferrari, P. Rath, R. Alaee, O. Kahl, V. Kovalyuk, S. Diewald, G. N. Goltsman, A. Korneev, C. Rockstuhl, and W. H. P. Pernice, Cavity-enhanced and ultrafast superconducting single-photon detectors, Nano Lett. **16**, 7085 (2016).

[20] J. Chiles, I. Charaev, R. Lasenby, M. Baryakhtar, J. Huang, A. Roshko, G. Burton, M. Colangelo, K. Van Tilburg, A. Arvanitaki, S. W. Nam, and K. K. Berggren, New constraints on dark photon dark matter with superconducting nanowire detectors in an optical haloscope, Phys. Rev. Lett. **128**, 231802 (2022). ISSN 0031-9007, 1079–7114.

[21] B. Korzh *et al.*, Demonstration of sub-3 ps temporal resolution with a superconducting nanowire single-photon detector, Nat. Photonics **14**, 250 (2020), ISSN 1749-4885, 1749-4893.

[22] A. Korneev, Yu. Korneeva, I. Florya, B. Voronov, and G. Goltsman, NbN nanowire superconducting single-photon detector for mid-infrared, Phys. Procedia **36**, 72 (2012), ISSN 18753892.

[23] F. Marsili, F. Bellei, F. Najafi, A. E. Dane, E. A. Dauler, R. J. Molnar, and K. K. Berggren, Efficient single photon detection from 500 nm to 5 mm wavelength, Nano. Lett. **12**, 4799 (2012), ISSN 1530-6984, 1530-6992.

[24] V. B. Verma, B. Korzh, A. B. Walter, A. E. Lita, R. M. Briggs, M. Colangelo, Y. Zhai, E. E. Wollman, A. D. Beyer, J. P. Allmaras, H. Vora, D. Zhu, E. Schmidt, A. G. Kozorezov, K. K. Berggren, R. P. Mirin, S. W. Nam, and M. D. Shaw, Single-photon detection in the mid-infrared up to 10μm wavelength using tungsten silicide superconducting nanowire detectors, APL Photonic **6**, 056101 (2021).

[25] M. Protte, V. B. Verma, J. P. Höpker, R. P. Mirin, S. W. Nam, and T. J. Bartley, Laser-lithographically written micron-wide superconducting nanowire single-photon detectors, Supercond. Sci. Technol. **35**, 055005 (2022), ISSN 0953-2048, 1361–6668.

[26] M. Lindgren, M. Currie, C. Williams, T. Y. Hsiang, P. M. Fauchet, R. Sobolewski, S. H. Moffat, R. A. Hughes, J. S. Preston, and F. A. Hegmann, Intrinsic picosecond response times of Y-Ba-Cu-O superconducting photodetectors, Appl. Phys. Lett. **74**, 853 (1999), ISSN 0003-6951, 1077-3118.

[27] D. F. Santavicca, Prospects for faster, higher-temperature superconducting nanowire single-photon detectors, Supercond. Sci. Technol. **31**, 040502 (2018), ISSN 0953-2048, 1361-6668.

[28] S. Charpentier, R. Arpaia, J. Gaudet, D. Matte, R. Baghdadi, T. Löfwander, D. Golubev, P. Fournier, T. Bauch, and F. Lombardi, Hot spot formation in electron-doped PCCO nanobridges, Phys. Rev. B **94**, 060503 (2016), ISSN 2469-9950, 2469-9969.

[29] H. Shibata, Photoresponse of a $La_{1.85}Sr_{0.15}CuO_4$ nanostrip, Supercond. Sci. Technol. **30**, 074001 (2017).

[30] P. Romano, M. Riccio, A. Guarino, N. Martucciello, G. Grimaldi, A. Leo, and A. Nigro, Electron doped superconducting cuprates for photon detectors, Measurement **122**, 502 (2018), ISSN 02632241.

[31] P. Amari, C. Feuillet-Palma, A. Jouan, F. Couëdo, N. Bourlet, E. Géron, M. Malnou, L. Méchin, A. Sharafiev, J. Lesueur, and N. Bergeal, High-temperature superconducting nano-meanders made by ion irradiation, Supercond. Sci. Technol. **31**, 015019 (2018), ISSN 0953-2048, 1361-6668.

[32] E. Andersson, R. Arpaia, E. Trabaldo, T. Bauch, and F. Lombardi, Fabrication and electrical transport characterization of high quality underdoped $YBa_2Cu_3O_{7-\delta}$ nanowires, Supercond. Sci. Technol. **33**, 064002 (2020), ISSN 0953-2048, 1361-6668.

[33] R. Arpaia, M. Ejrnaes, L. Parlato, F. Tafuri, R. Cristiano, D. Golubev, R. Sobolewski, T. Bauch, F. Lombardi, and G. P. Pepe, High-temperature superconducting nanowires for photon detection, Physica C **509**, 16 (2015).

[34] R. Arpaia, D. Golubev, R. Baghdadi, R. Ciancio, G. Dražić, P. Orgiani, D. Montemurro, T. Bauch, and F. Lombardi, Transport properties of ultrathin $YBa_2Cu_3O_{7-\delta}$ nanowires: A route to single photon detection, Phys. Rev. B **96**, 064525 (2017), ISSN 2469-9950, 2469-9969, Comment: 12 pages, 8 figures.

[35] M. Ejrnaes, L. Parlato, R. Arpaia, T. Bauch, F. Lombardi, R. Cristiano, F. Tafuri, and G. P. Pepe, Observation of dark pulses in 10 nm thick YBCO nanostrips presenting hysteretic current voltage characteristics, Supercond. Sci. Technol. **30**, 12LT02 (2017), ISSN 0953-2048, 1361-6668.

[36] M. Lyatti, M. A. Wolff, A. Savenko, M. Kruth, S. Ferrari, U. Poppe, W. Pernice, R. E. Dunin-Borkowski, and C. Schuck, Experimental evidence for hotspot and phase-slip mechanisms of voltage switching in ultrathin $YBa_2Cu_3O_{7-x}$ nanowires, Phys. Rev. B **98**, 054505 (2018), ISSN 2469-9950, 2469-9969.

[37] E. Trabaldo, R. Arpaia, M. Arzeo, E. Andersson, D. Golubev, F. Lombardi, and T. Bauch, Transport and noise properties of YBCO nanowire based nanoSQUIDs, Supercond. Sci. Technol. **32**, 073001 (2019), ISSN 0953-2048, 1361-6668.

[38] R. Arpaia, M. Ejrnaes, L. Parlato, R. Cristiano, M. Arzeo, T. Bauch, S. Nawaz, F. Tafuri, G. P. Pepe, and F. Lombardi, Highly homogeneous YBCO/LSMO nanowires for photoresponse experiments, Supercond. Sci. Technol. **27**, 044027 (2014), ISSN 0953-2048, 1361-6668.

[39] I. Charaev, D. A. Bandurin, A. T. Bollinger, I. Y. Phinney, I. Drozdov, M. Colangelo, B. A. Butters, T. Taniguchi, K. Watanabe, X. He, I. Božović, P. Jarillo-Herrero, and K. K. Berggren, Single-photon detection using high-temperature superconductors, Nat. Nanotech. 18, 343 (2023).

[40] R. Luque Merino, P. Seifert, J. Duran Retamal, R. Mech, T. Taniguchi, K. Watanabe, K. Kadowaki, R. H. Hadfield, and D. K. Efetov, Two-dimensional cuprate nanodetector with single telecom photon sensitivity at T = 20 K, 2D Mater. **10**, 021001 (2023).

[41] D. Hazra, N. Tsavdaris, S. Jebari, A. Grimm, F. Blanchet, F. Mercier, E. Blanquet, C. Chapelier, and M. Hofheinz, Superconducting properties of very high quality NbN thin films grown by high temperature chemical vapor deposition, Supercond. Sci. Technol. **29**, 105011 (2016).

[42] M. Sidorova, A. Semenov, H.-W. Hübers, K. Ilin, M. Siegel, I. Charaev, M. Moshkova, N. Kaurova, G. N. Goltsman, X. Zhang, and A. Schilling, Electron energy relaxation in disordered superconducting NbN films, Phys. Rev. B **102**, 054501 (2020).

[43] A. J. Annunziata, O. Quaranta, D. F. Santavicca, A. Casaburi, L. Frunzio, M. Ejrnaes, M. J. Rooks, R. Cristiano, S. Pagano, A. Frydman, and D. E. Prober, Reset dynamics and latching in niobium superconducting nanowire single-photon detectors, J. Appl. Phys. **108**, 084507 (2010), ISSN 0021-8979, 1089-7550.

[44] R. Sobolewski, in *Superconducting and Related Oxides: Physics and Nanoengineering IIIa*, edited by Davor Pavuna and Ivan Bozovic (1998), p. 480.

[45] D. Yu. Vodolazov, Single-photon detection by a dirty current-carrying superconducting strip based on the kinetic-equation approach, Phys. Rev. Appl. **7**, 034014 (2017), ISSN 2331-7019.

[46] N. Barišić, M. K. Chan, Y. Li, G. Yu, X. Zhao, M. Dressel, A. Smontara, and M. Greven, Universal sheet resistance and revised phase diagram of the cuprate high-temperature superconductors, Proc. Natl. Acad. Sci. **110**, 12235 (2013).

[47] R. P. Gupta and M. Gupta, Order-disorder-driven change in hole concentration and superconductivity in $YBa_2Cu_3O_{6.5}$, Phys. Rev. B **44**, 2739 (1991), ISSN 0163-1829, 1095-3795.

[48] C. C. Tsuei, J. R. Kirtley, C. C. Chi, L. S. Yu-Jahnes, A. Gupta, T. Shaw, J. Z. Sun, and M. B. Ketchen, Pairing symmetry and flux quantization in a tricrystal superconducting ring of $YBa_2Cu_3O_{7-\delta}$, Phys. Rev. Lett. **73**, 593 (1994), ISSN 0031-9007.

[49] D. A. Wollman, D. J. Van Harlingen, W. C. Lee, D. M. Ginsberg, and A. J. Leggett, Experimental determination of the superconducting pairing state in YBCO from the phase coherence of YBCO-Pb dc SQUIDs, Phys. Rev. Lett. **71**, 2134 (1993), ISSN 0031-9007.

[50] J. Lesueur, P. Nedellec, H. Bernas, J. P. Burger, and L. Dumoulin, Depairing-like variation of T_c in $YBa_2Cu_3O_{7-\delta}$, Phys. C: Superconductivity **167**, 1 (1990), ISSN 0921-4534.

[51] H. Assink, A. J. M. Harg, C. M. Schep, N. Y. Chen, D. Marel, P. Hadley, E. W. J. M. Drift, and J. E. Mooij, Critical currents in submicron YBa/sub 2/Cu/sub 3/O/sub 7/ lines, IEEE Trans. Appl. Supercond. **3**, 2983 (1993), ISSN 1558-2515.

[52] P. Larsson, B. Nilsson, and Z. G. Ivanov, Fabrication and transport measurements of $YBa_2Cu_3O_{7-x}$ nanostructures, J. Vac. Sci. Technol. B **18**, 8 (2000).

[53] S. Nawaz, Ph.D. thesis, Chalmers University of Technology, Sweden, 2013.

[54] S. K. H Lam, A. Bendavid, and J. Du, Hot spot formation in focused-ion-beam-fabricated $YBa_2Cu_3O_{7-x}$ nanobridges with high critical current densities, Nanotechnology **30**, 325301 (2019), ISSN 0957-4484, 1361-6528.

[55] G. Papari, F. Carillo, D. Stornaiuolo, L. Longobardi, F. Beltram, and F. Tafuri, High critical current density and scaling of phase-slip processes in YBaCuO nanowires, Supercond. Sci. Technol. **25**, 035011 (2012), ISSN 0953-2048, 1361-6668.

[56] G. Papari, F. Carillo, D. Stornaiuolo, D. Massarotti, L. Longobardi, F. Beltram, and F. Tafuri, Dynamics of vortex matter in YBCO sub-micron bridges, Physica C: Superconductivity Applications **506**, 188 (2014), ISSN 09214534.

[57] R. Arpaia, S. Nawaz, F. Lombardi, and T. Bauch, 23(3):1101505–1101505. ISSN 1558–2515.

[58] N. Curtz, E. Koller, H. Zbinden, M. Decroux, and L. Antognazza, Patterning of ultrathin YBCO nanowires using a new focused-ion-beam process, Supercond. Sci. Technol. **23**, 045015 (2010).

[59] M. Lyatti, A. Savenko, and U. Poppe, Ultra-thin $YBa_2Cu_3O_{7-x}$ films with high critical current density, Supercond. Sci. Technol. **29**, 065017 (2016), ISSN 0953-2048, 1361-6668.

[60] Y. Maeno, T. Tomita, M. Kyogoku, S. Awaji, Y. Aoki, K. Hoshino, A. Minami, and T. Fujita, Substitution for copper in a high-T_c superconductor $YBa_2Cu_3O_{7-\delta}$, Nature **328**, 512 (1987), ISSN 0028-0836.

[61] S. A. Cybart, E. Y. Cho, T. J. Wong, B. H. Wehlin, M. K. Ma, C. Huynh, and R. C. Dynes, Nano Josephson superconducting tunnel junctions in $YBa_2Cu_3O_{(7-\delta)}$ directly patterned with a focused helium ion beam, Nat. Nanotechnol. **10**, 598 (2015).

[62] C.-H. Chen, I. Jin, S. P. Pai, Z. W. Dong, R. P. Sharma, C. J. Lobb, T. Venkatesan, K. Edinger, J. Orloff, J. Melngailis, Z. Zhang, and W. K. Chu, Combined method of focused ion beam milling and ion implantation techniques for the fabrication of high temperature superconductor Josephson junctions, J. Vac. Sci. Technol. B **16**, 2898 (1998).

[63] T. J. Tate, M. J. Lee, Y. Li, J. A. Kilner, Y. H. Li, C. A. Leach, D. Lacey, A. D. Caplin, R. E. Somekh, P. Przyslupski, and P. G. Quincey, Crystal regrowth of YBCO thin films by ion implantation and rapid thermal annealing, Physica C: Superconductivity **235**, 569 (1994), ISSN 0921–4534.

[64] F. Couedo, P. Amari, C. Feuillet-Palma, C. Ulysse, Y. K. Srivastava, R. Singh, N. Bergeal, and J. Lesueur, Dynamic properties of high-T_c superconducting nano-junctions made

with a focused helium ion beam, Sci. Rep. **10**, 106001–9 (2020).
[65] R. C. Jaeger, *Number v. 5 in Modular Series on Solid State Devices* (Prentice Hall, Upper Saddle River, New Jersey, 2002), 2nd ed., ISBN 978-0-201-44494-0.
[66] J. Lesueur, S. Degoy, M. Aprili, D. Chambonnet, and D. Keller, in *Photonics West '96*, edited by Ivan Bozovic and Davor Pavuna (San Jose, California, 1996), p. 250.
[67] N. Bergeal, X. Grison, J. Lesueur, G. Faini, M. Aprili, and J. P. Contour, High-quality planar high-T_c Josephson junctions, Appl. Phys. Lett. **87**, 102502 (2005).
[68] N. Bergeal, J. Lesueur, G. Faini, M. Aprili, and J. P. Contour, High T_c superconducting quantum interference devices made by ion irradiation, Appl. Phys. Lett. **89**, 112515 (2006).
[69] F. Couedo, E. R. Pawlowski, J. Kermorvant, J. Trastoy, D. Crété, Y. Lemaître, B. Marcilhac, C. Ulysse, C. Feuillet-Palma, N. Bergeal, and J. Lesueur, High-T_c superconducting detector for highly-sensitive microwave magnetometry, Appl. Phys. Lett. **114**, 192602 (2019).
[70] J. Lesueur, N. Bergeal, M. Sirena, X. Grison, G. Faini, M. Aprili, and J. P. Contour, High T_c Josephson nanojunctions made by ion irradiation: Characteristics and reproducibility, IEEE Trans. Appl. Supercond. **17**, 963 (2007).
[71] M. Malnou, A. Luo, T. Wolf, Y. Wang, C. Feuillet-Palma, C. Ulysse, G. Faini, P. Febvre, M. Sirena, J. Lesueur, and N. Bergeal, Toward terahertz heterodyne detection with superconducting Josephson junctions, Appl. Phys. Lett. **101**, 233505 (2012).
[72] M. Malnou, C. Feuillet-Palma, C. Ulysse, G. Faini, P. Febvre, M. Sirena, L. Olanier, J. Lesueur, and N. Bergeal, High-T_c superconducting Josephson mixers for terahertz heterodyne detection, J. Appl. Phys. **116**, 074505 (2014).
[73] E. R. Pawlowski, J. Kermorvant, D. Crété, Y. Lemaître, B. Marcilhac, C. Ulysse, F. Couedo, C. Feuillet-Palma, N. Bergeal, and J. Lesueur, Static and radio frequency magnetic response of high T_c superconducting quantum interference filters made by ion irradiation, Supercond. Sci. Technol. **31**, 095005–11 (2018).
[74] A. Sharafiev, M. Malnou, C. Feuillet-Palma, C. Ulysse, P. Febvre, J. Lesueur, and N. Bergeal, Josephson oscillation linewidth of ion-irradiated $YBa_2Cu_3O_7$ junctions, Supercond. Sci. Technol. **29**, 074001 (2016).
[75] A. Sharafiev, M. Malnou, C. Feuillet-Palma, C. Ulysse, T. Wolf, F. Couëdo, P. Febvre, J. Lesueur, and N. Bergeal, HTS Josephson junctions arrays for high-frequency mixing, Supercond. Sci. Technol. **31**, 035003–9 (2018).
[76] J. F. Ziegle and J. P. Biersack, *The Stopping and Range of Ions in Matter* (IBM, New York, 2004).
[77] https://www.microresist.de/ (2022).
[78] R. Arpaia, Ph.D. thesis, Chalmers University of Technology, Sweden, 2016.
[79] J. Bardeen, Critical fields and currents in superconductors, Rev. Mod. Phys. **34**, 667 (1962), ISSN 0034-6861.
[80] W. J. Skocpol, M. R. Beasley, and M. Tinkham, Self-heating hotspots in superconducting thin-film microbridges, J. Appl. Phys. **45**, 4054 (1974), ISSN 0021-8979, 1089-7550.
[81] R. P. Huebener, Self-heating effects in thin-film type-I superconductors, J. Appl. Phys. **46**, 5 (2014).
[82] D. K. Liu, L. X. You, S. J. Chen, X. Y. Yang, Z. Wang, Y. L. Wang, X. M. Xie, and M. H. Jiang, Electrical characteristics of superconducting nanowire single photon detector, IEEE Trans. Appl. Supercond. **23**, 2200804 (2013), ISSN 1558-2515.
[83] J. P. Maneval, K. Harrabi, F. Chibane, M. Rosticher, F. R. Ladan, and P. Mathieu, Temperature profile of hotspots in narrow current-biased superconducting strips, IEEE Trans. Appl. Supercond. **23**, 2200604 (2013), ISSN 1051-8223, 1558-2515.
[84] D. Golubev, F. Lombardi, and T. Bauch, Effect of heating on critical current of YBCO nanowires, Physica C: Superconductivity Applications **506**, 174 (2014), ISSN 0921-4534.
[85] A. Sergeev, A. Semenov, V. Trifonov, B. Karasik, G. Gol'tsman, and E. Gershenzon, Heat transfer in YBaCuO thin film/sapphire substrate system, J. Supercond. **7**, 341 (1994), ISSN 0896-1107, 1572-9605.
[86] M. Nahum, S. Verghese, P. L. Richards, and K. Char, Thermal boundary resistance for $YBa_2Cu_3O_{7-\delta}$ films, Appl. Phys. Lett. **59**, 2034 (1991), ISSN 0003-6951, 1077-3118.
[87] T. Klitsner and R. O. Pohl, Phonon scattering at silicon crystal surfaces, Phys. Rev. B **36**, 6551 (1987), ISSN 0163-1829.
[88] W. A. Little, (Springer US, Boston, Massachusetts, 1996), p. 15, ISBN 978-1-4613-0411-1.
[89] J. Ashkenazi, S. E. Barnes, F. Zuo, G. C. Vezzoli, and B. M. Klein, editors. (Springer US, Boston, Massachusetts, 1991), ISBN 978-1-4613-6471-9 978-1-4615-3338-2.
[90] M. Matsukawa, T. Mizukoshi, K. Noto, and Y. Shiohara, Thermal conductivity in the *ab*-plane of a large single crystal $YBa_2Cu_3O_{7-\delta}$ with several oxygen contents, J. Low. Temp. Phys. **105**, 987 (1996), ISSN 1573-7357.
[91] R. C. Yu, M. B. Salamon, J. P. Lu, and W. C. Lee, Thermal conductivity of an untwinned $YBa_2Cu_3O_{7-\delta}$ single crystal and a new interpretation of the superconducting state thermal transport, Phys. Rev. Lett. **69**, 1431 (1992), ISSN 0031-9007.